UNIVERSITY OF CALIFORNIA SAN DIEGO

Optimization of Thin Film Solid Electrolytes for Energy Storage

A Thesis submitted in partial satisfaction of the requirements
for the degree Master of Science

in

Nanoengineering

by

Randall Burger

Committee in charge:

Professor Y. Shirley Meng, Chair
Professor David Fenning, Co-chair
Professor Jesse Jokerst

2023

The Thesis of Randall Burger is approved, and it is acceptable in quality and form for publication on microfilm and electronically.

University of California San Diego

2023

DEDICATION

This is for my father, who has always supported me. You have taught me to reach for my dreams, and I now have the confidence to pull them into reality.

TABLE OF CONTENTS

LIST OF FIGURES

LIST OF TABLES

ACKNOWLEDGEMENTS

I’d like to acknowledge my advisor, Professor Y. Shirley Meng, for lending me the opportunity to join a highly accomplished research group.

I’d like to acknowledge my mentor Ryosuke Shimizu, whose guidance has facilitated my growth as an engineer and scholar.

ABSTRACT OF THE THESIS

Optimization of Thin Film Solid Electrolytes for Energy Storage

by

Randall Burger

Master of Science in Nanoengineering

University of California San Diego, 2023

Professor Y. Shirley Meng, Chair

Professor David Fenning, Co-chair

Thin film LiPON and LLTO are promising solid electrolyte candidates in the development of next generation batteries. These materials can be deposited via RF magnetron sputtering, which is a technique suitable for thin film mass production. In this work, the deposition conditions for LiPON and LLTO are optimized to improve film quality. The thickness of LiPON films is shown to be tunable with the approximation of deposition rate.

LiPON films as thin as 325 nm are produced to exhibit sufficient ionic conductivity and low electronic conductivity. Strong electrochemical performance means LiPON can remain a cohesive film even at very thin scales. With this, LiPON has potential to improve volumetric energy density when implemented into thin film batteries. Bulk LLTO is characterized to relate ionic conductivity to Li amount, and the composition with highest ionic conductivity influences the choice of LLTO sputtering target. LLTO film deposition rate is studied as a function of both RF power and deposition pressure, and RF power is shown to have a much stronger effect on deposition rate. Film delamination issues are addressed by decreasing LLTO film thickness, and adhesion to the Si substrate is maintained during the post annealing process. EDS analysis yields the La/Ti ratios of LLTO films, illustrating changes in LLTO composition due to deposition pressure.

CHAPTER 1. INTRODUCTION

All-solid-state batteries (ASSBs) have attracted great interest because of their properties. ASSB assembly entails the stacking of solid electrodes with a solid state electrolyte (SSE) material in between, the SSE acting as both a separator and a host of lithium diffusion pathways.[1,2] Consisting of only solid phase components, such batteries display large thermal stability windows and no risk of leakage.[1-3] These inherent safety advantages motivate the development of ASSBs for energy storage applications. In addition, ASSBs can be scaled down to the thin film level with current manufacturing methods. Although they have reduced overall capacity, thin film Li ion batteries have displayed fast charging capabilities and long cycle lifetimes, which are important traits for microdevice implementation.[2] With goals to miniaturize and integrate various devices, the Internet of Things movement can be further enabled by microscale energy storage technologies.[1-3]

The specific choice of SSE material is critical to the success of thin film ASSB systems. To reduce charge transfer resistance in Li ion diffusion, it is a requirement for electrolyte materials to have sufficient ionic conductivity. Currently, liquid electrolytes have significantly larger ionic conductivities than that of SSEs, so a large focus has been to improve the Li ion conductivity of the latter.[2] One extensively studied SSE is amorphous lithium phosphorous oxynitride, known as LiPON. LiPON exhibits a wide electrochemical stability window of 5.5 V, ionic conductivity of ~10^{-6} S/cm, and a low electronic conductivity of ~10^{-12}-10^{-13} S/cm.[3-5] One of the most common methods to fabricate LiPON is by RF magnetron sputtering, a physical vapor deposition technique known to produce highly uniform and dense thin films.[2]

Another promising SSE is amorphous lithium lanthanum titanate, or LLTO. When synthesized in amorphous form, LLTO can achieve high ionic conductivities. This has

previously been shown in the study of LLTO thin films grown by pulsed laser deposition (PLD). By controlling oxygen gas pressure and the substrate temperature during deposition, LLTO thin films can reach 3.0×10^{-4} S/cm ionic conductivity.[6] There have also been numerous efforts to optimize LLTO by sputtering deposition, with ionic conductivities from this method reaching up to 5.32×10^{-5} S/cm with the addition of post annealing.[7-10] This is not as high as PLD because it tends to be more difficult to control the chemical composition of films with sputtering, while PLD employs high energy and directionality of deposition. However, a major advantage of sputtering is that it doesn't require a high-powered laser, so it offers greater scalability for thin film battery manufacturing. As such, there is incentive to further optimize the sputtering process to produce higher quality LLTO films.

This work describes the optimization of LiPON and LLTO sputtering conditions for thin film ASSB applications. With LiPON, sputtered film thickness will be tuned, and conductivity values of LiPON will be investigated as film thickness is decreased. For LLTO, the sputtering target composition with the potential to produce high ionic conductivity films will be investigated. Thin film LLTO morphology will be characterized to ensure film adhesion, and changes in film chemistry will be monitored.

CHAPTER 2. EXPERIMENTAL

LiPON Thin Film Preparation: LiPON thin films were each deposited onto platinum coated silicon substrates with RF magnetron sputtering. A Li_3PO_4 sputtering target was used for LiPON, while a $Li_{0.68}La_{0.49}TiO_3$ target was used for LLTO. Each sputtering target had a diameter of approximately 50 mm. For LiPON, deposition was performed with nitrogen gas (ultra high purity) at partial pressure of 12 mTorr. RF sputtering power was set to 50 W. The Li_3PO_4 target was pre-sputtered for 1 hour to remove surface impurities before starting film deposition. Four copper electrodes (2 mm × 2 mm each) were thermally evaporated on top of LiPON to form solid Cu/LiPON/Pt cells.

Bulk LLTO Solid State Synthesis: Bulk LLTO has the formula $Li_{3X}La_{(2-X)/3}TiO_3$. Precursor powders of Li_2CO_3, TiO_2, and La_2O_3 were mixed by hand to make LLTO compositions of different lithium amounts (3X = 0.1, 0.2, 0.3, 0.4, and 0.5). Each mixture was ball-milled at 400 rpm for 4 hrs. The mixtures were calcinated inside a box furnace at 1200 °C for 6 hrs. Each LLTO mixture was re-ground by hand, then pelletized under a hydraulic press with a 1/2 “ die. Powders were compressed under 10 tons of pressure for 5 mins to form pellet structures. The pellets were then sintered inside a box furnace at 1500 °C for 5 hrs. Gold electrodes were sputtered onto each side of the pellets to form Au/LLTO/Au cells for electrochemical measurement.

LLTO Thin Film Preparation: For LLTO, thin films were sputtered onto platinum coated silicon substrates. Deposition was in the presence of Ar and O_2 gasses, with the Ar:O_2 volume ratio kept at 70:30. Various depositions were performed at 50 W and 80 W RF power. The $Li_{0.68}La_{0.49}TiO_3$ target was pre-sputtered for 1 hour to remove any potential surface contaminants. LLTO films were post annealed in a box furnace at 300 °C for 2 hours.

Electrochemical Measurement: Measurements were conducted with a Biologic SP-200 potentiostat. Electrochemical impedance spectroscopy (EIS) measurements were in the frequency range 3 MHz to 3 Hz. DC polarization measurements for Cu/LiPON/Pt cells were set at 1 V bias over a duration of 10 minutes.

CHAPTER 3. RESULTS AND DISCUSSION

3.1. LiPON Film Thickness Tuning

To attain control of film growth to specific thicknesses, LiPON films were grown for various deposition times to estimate the deposition rate. These films are shown in Fig. 3.1. The deposition times of films (a), (b), and (c) were chosen to target thicknesses of 1000 nm, 500 nm, and 250 nm, respectively. With stark differences between the measured and target values, it was evident that calibration was needed. Utilizing the calculation of a new deposition rate, LiPON films (d), (e), and (f) were grown to target 1000 nm, 500 nm, and 250 nm. Compared to previous films, their measured thicknesses were closer to the target values.

A new sputtering deposition rate for LiPON was established by calibrating with consideration to each of the films made. In Fig. 3.1, we can see that a linear fit is a good descriptor of the relationship between deposition time and film thickness. This is not a perfect model, clearly noted by the intercept value of the fit line. This is because the non-linear island growth mechanism is prominent at short deposition times and is eventually taken over by film growth as deposition proceeds.[11] As such, we can approximate the film growth of LiPON to be a linear phenomenon, with the deposition rate given by the equation of the fit line. With the recalibrated data, we possess the ability to finely tune the thickness of LiPON.

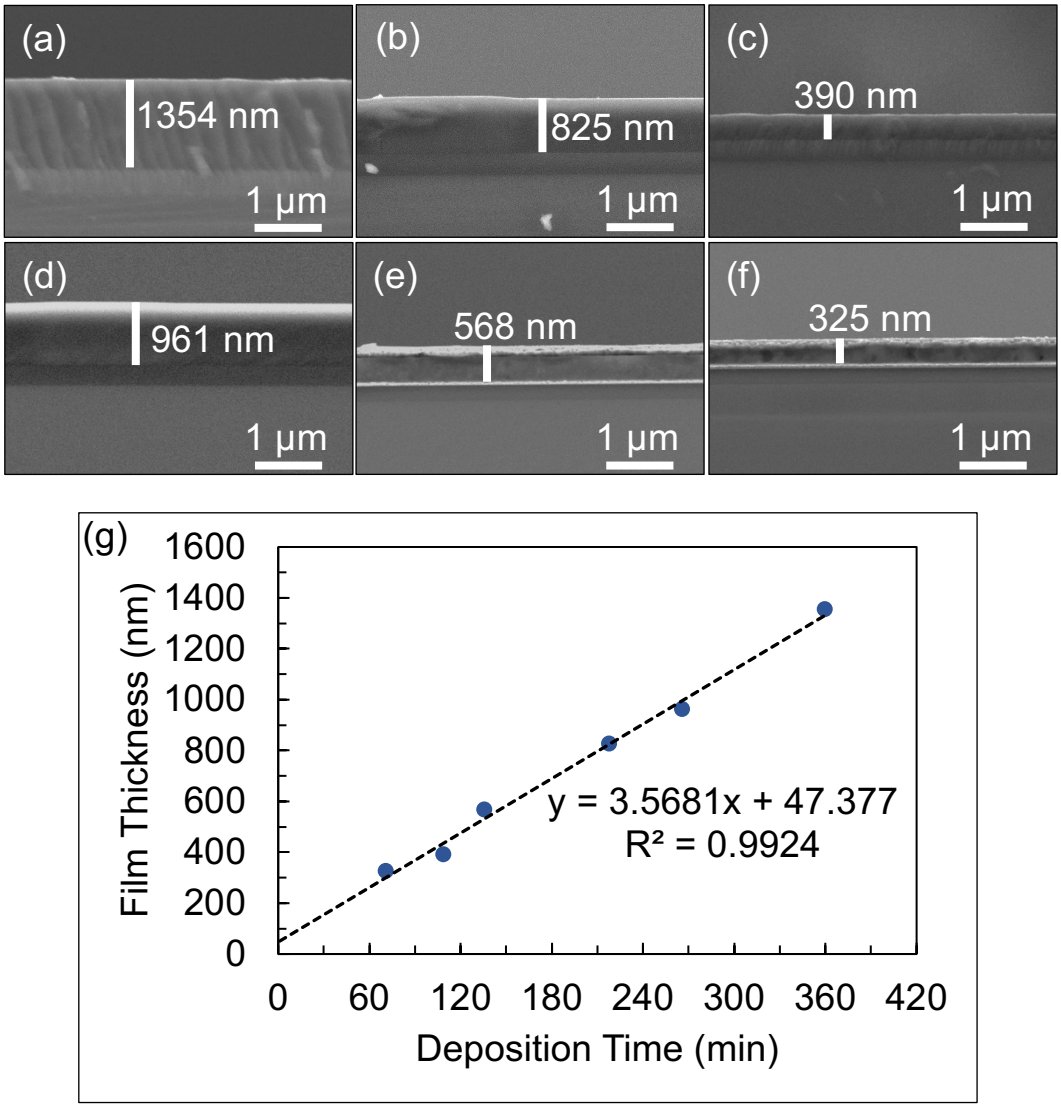

Figure 3.1: Cross sectional SEM images of LiPON films deposited for (a) 360 mins, (b) 218 mins, (c) 109 mins, (d) 266 mins, (e) 136 mins, and (f) 71 mins. Each film corresponds to a point in (g), which displays LiPON film thickness as a function of deposition time. A linear fit describes the relationship.

3.2. LiPON Electrochemical Testing

A Cu/LiPON/Pt cell was made with each LiPON sample. The EIS responses of the cells are shown in Fig. 3.2. No electrochemical data was collected from the 390 nm LiPON sample because each measurement point on the cell was short circuited. The single semicircle response we see from the measured films means there is impedance associated with the electrolyte

material. In this case, real impedance values correspond to ionic resistance. As the LiPON films are grown thinner, we see that the ionic resistance decreases. In DC polarization measurements, the large initial drops in current signify the blocking of ionic current. The electronic leakage current was collected after 10 mins and is of interest to us because it represents the degree of electron resistance through the LiPON. We find that all LiPON films exhibited a leakage current of < 2 nA.

Using the ionic resistance and the electronic leakage current, we can calculate the ionic and electronic conductivities of LiPON at each film thickness. Conductivity values were calculated with the following equation.

$$\sigma = \frac{L}{RA} \qquad [1]$$

Here, σ represents the conductivity, L the film thickness, R the film resistance, and A the electrode area. Selecting R to be the ionic resistance of LiPON, we can calculate the ionic conductivity. Similarly, Ohm's Law is utilized to calculate the electronic resistance of LiPON from leakage current values, and the use of electronic resistance in Eqn. 1 yields electronic conductivity. Conductivity values for each thickness result from averaging data from multiple measurement sites on the same LiPON film. These values are shown in Table 3.1. There are no standard deviation values for the 825 nm LiPON sample because there was short circuiting on all but one measurement site for the cell.

LiPON conductivities are visualized as a function of thickness in Fig. 3.3. We see that ionic conductivity remains on the order of 10^{-6} S/cm regardless of the thickness of LiPON. This coincides with what has been predicted in previous literature.[4] There are also clear order of

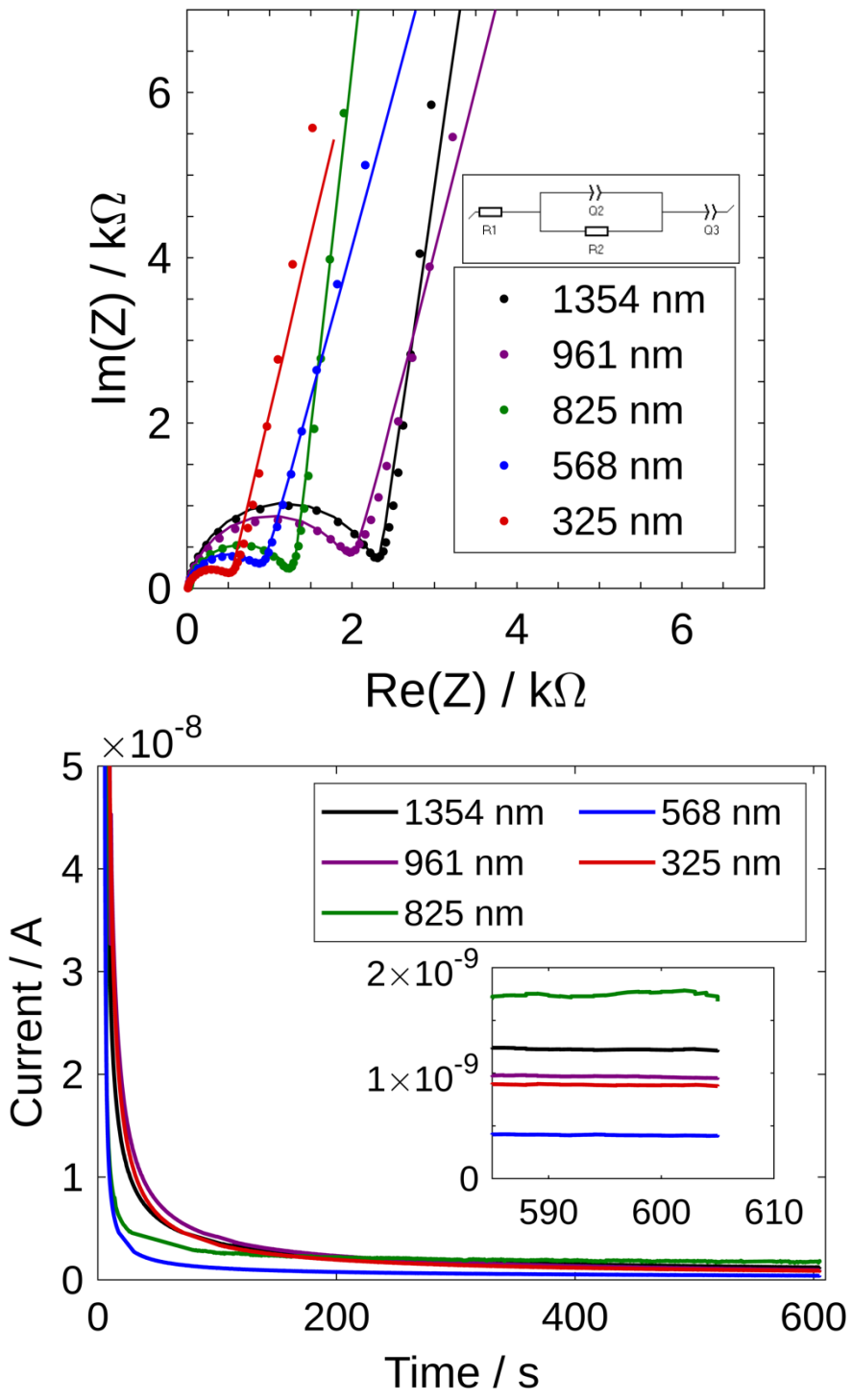

Figure 3.2: Electrochemical measurements for LiPON films of different thickness. The EIS plots (top) were fitted to the equivalent circuit shown. DC polarization tests (bottom) were conducted at 1 V.

Table 3.1: Average ionic (σ_i) and electronic (σ_e) conductivities for LiPON films of various thickness, with their respective standard deviations (s_i , s_e).

Thickness (nm)	σ_i (S/cm)	s_i (S/cm)	σ_e (S/cm)	s_e (S/cm)
1354	1.76×10^{-6}	0.26×10^{-6}	3.78×10^{-12}	3.24×10^{-12}
961	1.30×10^{-6}	0.09×10^{-6}	3.87×10^{-12}	2.35×10^{-12}
825	1.64×10^{-6}	-	3.56×10^{-12}	-
568	1.61×10^{-6}	0.05×10^{-6}	8.55×10^{-13}	5.57×10^{-13}
325	1.62×10^{-6}	0.12×10^{-6}	1.06×10^{-13}	1.04×10^{-13}

magnitude differences between the LiPON ionic and electronic conductivities at each film thickness. This means that the LiPON films remain cohesive and without breakage, while exhibiting strong electrochemical properties. Here I report that LiPON can be utilized as an effective solid state electrolyte material even at 325 nm thick. This reinforces the favorability of LiPON for ASSB applications because its capabilities as an electrolyte could be maintained while taking up less space in the cell. This provides avenues to increase the volumetric energy density of ASSBs with LiPON, as this allows the overall cell size to be reduced, or the growth of thicker electrode materials to improve cell capacity.

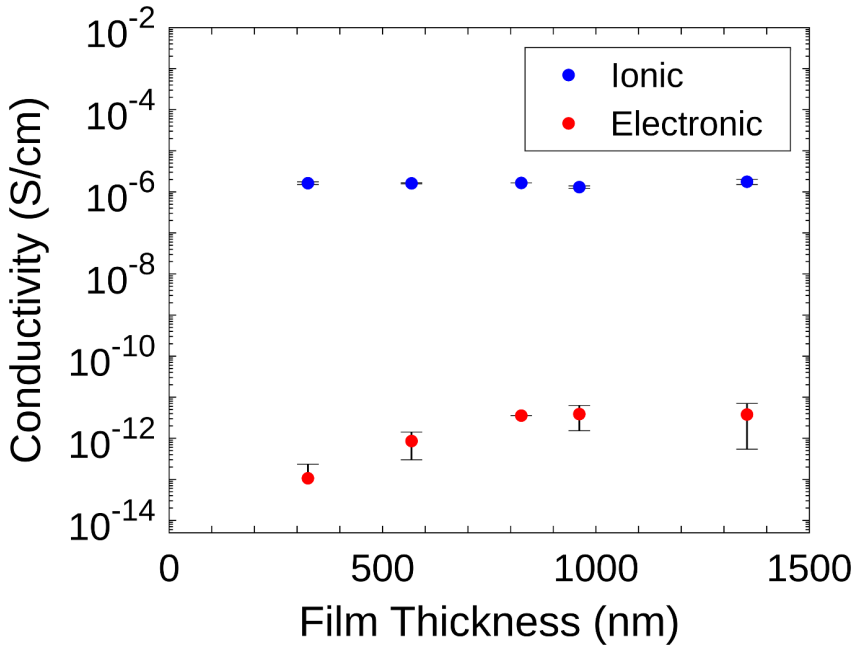

Figure 3.3: LiPON ionic and electronic conductivity as a function of film thickness.

3.3. LLTO Bulk Composition Study

With sputtering, it is desired for composition to transfer from the bulk target material to the film. For LLTO film making, a favorable target is one which yields high bulk ionic conductivity. The bulk LLTO pellets made for each lithium amount were measured with EIS, and a similar response was observed for each lithium amount. An example can be seen in Fig. 3.4. The EIS plot here is of the LLTO pellet with lithium content 3X = 0.4. We see definition from two semicircles in the response of bulk LLTO. The semicircle of higher frequency can be attributed to bulk resistance, while that of the lower frequency is resistance from grain boundaries in the material. Here, the bulk resistance is used to calculate ionic conductivity.

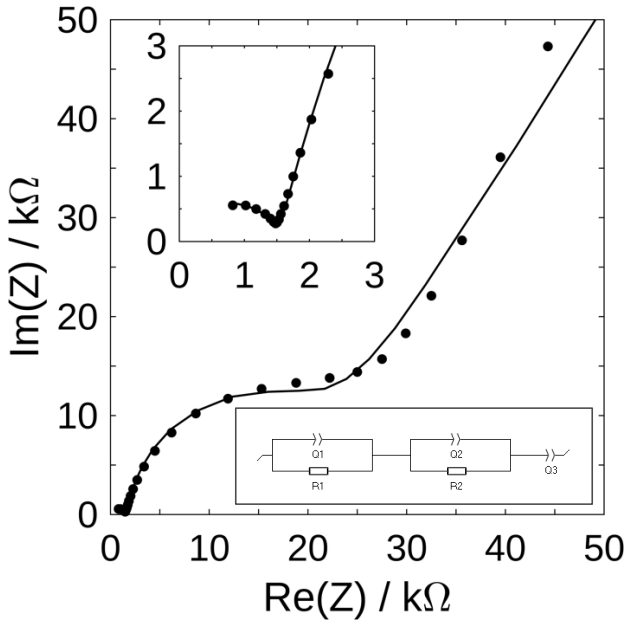

Figure 3.4: EIS spectra of the LLTO pellet with lithium amount 3X = 0.4. The response is fitted to the equivalent circuit shown.

Ionic conductivities of each bulk LLTO composition were calculated via Eqn. 1, using measured pellet thicknesses and electrode areas. Bulk LLTO ionic conductivity is plotted with respect to lithium content in Fig. 3.5. The LLTO pellet with lithium content 3X = 0.4 provided the largest average ionic conductivity of 0.93×10^{-3} S/cm. Ion conductivity is enhanced as lithium amount increases from 3X = 0.1 to 0.4, a trend which agrees with a past study involving similar LLTO compositions.[12] In selecting the composition of the LLTO target, the lithium amount 3X = 0.4 is the lower limit for lithium needed in the target. This is because we must consider lithium loss during the sputtering process and film annealing. Lithium has relatively low atomic mass, meaning there is a higher chance for lithium to be scattered in the deposition chamber. This often results in the sputtered film composition containing less lithium compared to the target material. In addition, lithium can be evaporated from the film during annealing, reducing lithium amount in the film as well as ionic conductivity. To compensate for this expected loss, an LLTO target

with lithium content greater than 3X = 0.4 was selected. We purchased a $Li_{0.68}La_{0.49}TiO_3$ target (lithium amount 3X = 0.68) for LLTO deposition.

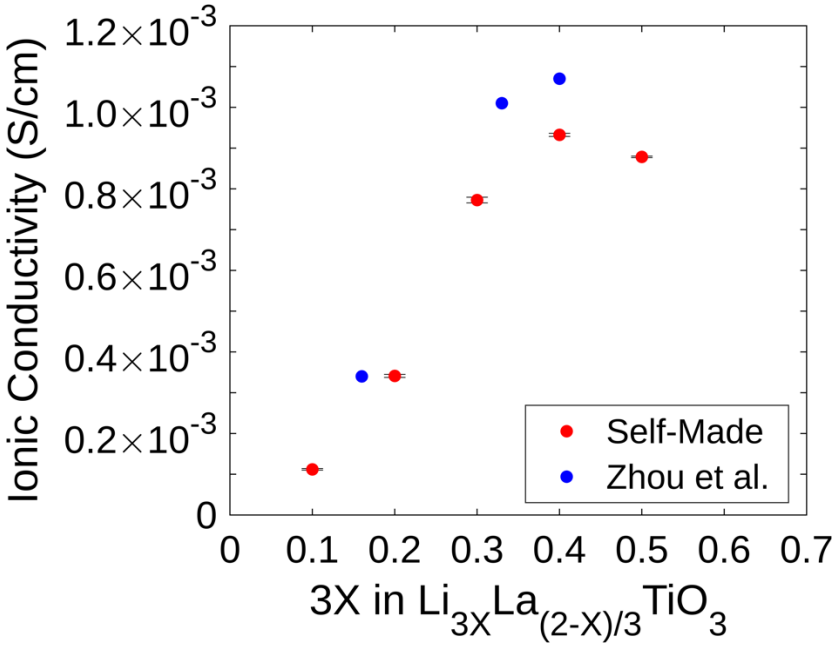

Figure 3.5: Bulk ionic conductivity of LLTO as a function of lithium amount. Self-made LLTO pellets in this study are compared to similar compositions measured by Zhou et al.[12]

3.4. LLTO Film Deposition and Morphology

The first metric explored here is the deposition rate of sputtered LLTO. Six LLTO samples were prepared with deposition time fixed at 1 hr 30 mins. The samples consisted of amorphous LLTO grown at an RF power of 50 W and 80 W, at the pressures 7.5 mTorr, 10 mTorr, and 15 mTorr. Fig. 3.6 displays cross sectional SEM images of the LLTO films grown with 7.5 mTorr pressure. With the same deposition time and pressure, we see that sputtering with 80 W power produces a thicker film than with 50 W. Under the deposition pressure of 7.5 mTorr, we find the deposition rate to be 5.8 ± 0.1 nm/min at 80 W, and 3.7 ± 0.1 nm/min at 50 W. Greater deposition power also enhances deposition rate when sputtering LLTO at 10 mTorr and

15 mTorr. However, the effect of deposition pressure on LLTO deposition rate is negligible for the samples tested here.

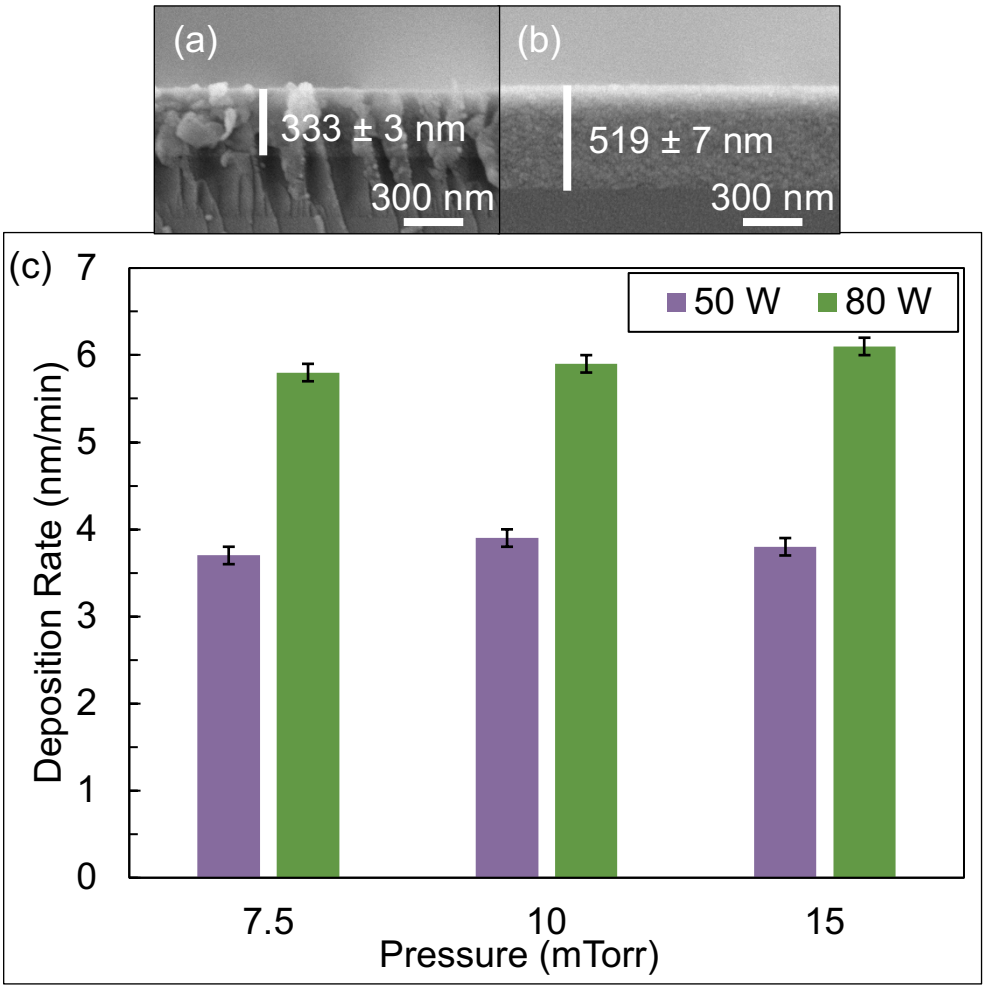

Figure 3.6: SEM images of LLTO deposited at 7.5 mTorr, one at (a) 50 W, the other at (b) 80 W. Sputtering deposition rates for LLTO at different power and pressure are shown in (c).

It is evident that adjusting RF power has a much stronger influence over LLTO deposition rate. This makes sense when considering the effect of these deposition parameters on the sputtering mechanism. By increasing RF power, the kinetic energy of ionized gas is increased during sputtering. As a result, ionized gas impacting the target sputter off larger particle sizes to be deposited in the film. When the deposition pressure is increased, there is a greater amount of

gas impacting the target at any given time. This increases the efficiency of deposition because of increased collisions, but this benefit is counteracted by a reduced mean free path of particles in the chamber, which increases the likelihood of scattering events and slows deposition rate.

Having tuned the deposition rate, I proceeded to make LLTO thin films. Deposition time was set to 164 mins with the goal to make 1 μm thick LLTO. However, issues arose after the annealing process. Visible morphological nonuniformities were observed on each sample. Two deposition conditions were examined to address this issue, LLTO deposited at 7.5 mTorr and at 15 mTorr. Surface SEM images were taken along the divide between morphological regions, and EDS mapping revealed the local chemistry. Fig. 3.7 displays the signals gathered from the 15 mTorr LLTO sample. We see that the La, Ti, and O signals associated with LLTO are strongly present only on one side of the divide. Likewise, the Si and Pt signals associated with the substrate are strongly present on the opposing side of the divide. From this, we can confirm that regions of the LLTO film are damaged as a result of film delamination.

In addressing film delamination, it is necessary to consider the coefficient of thermal expansion (CTE) of both the substrate and film. When there is a large mismatch between CTE values, the substrate and film expand and contract at different rates while they are heated and cooled, causing stress at the interface. LLTO has a CTE of 1.0×10^{-5} K^{-1}, while the single crystal silicon substrate has a CTE of 2.6×10^{-6} K^{-1}.[13, 14] This large mismatch in CTE is a likely the cause of film delamination. There are approaches we can take to reduce the stress at the interface. One option is to change the substrate to another material. For example, alumina has a CTE of 8.0×10^{-6} K^{-1}, so using it as a substrate for LLTO would lessen the mismatch and reduce interfacial stress.[15] Another option is to keep the Si substrate but make thinner films. Such an approach may lessen the severity of the stress gradient through the film as it is annealed on the

substrate. I opted for the latter approach, targeting an LLTO film thickness of 500 nm instead of 1 μm. Deposition time was adjusted to 82 mins. After annealing, no damage was observed on the films.

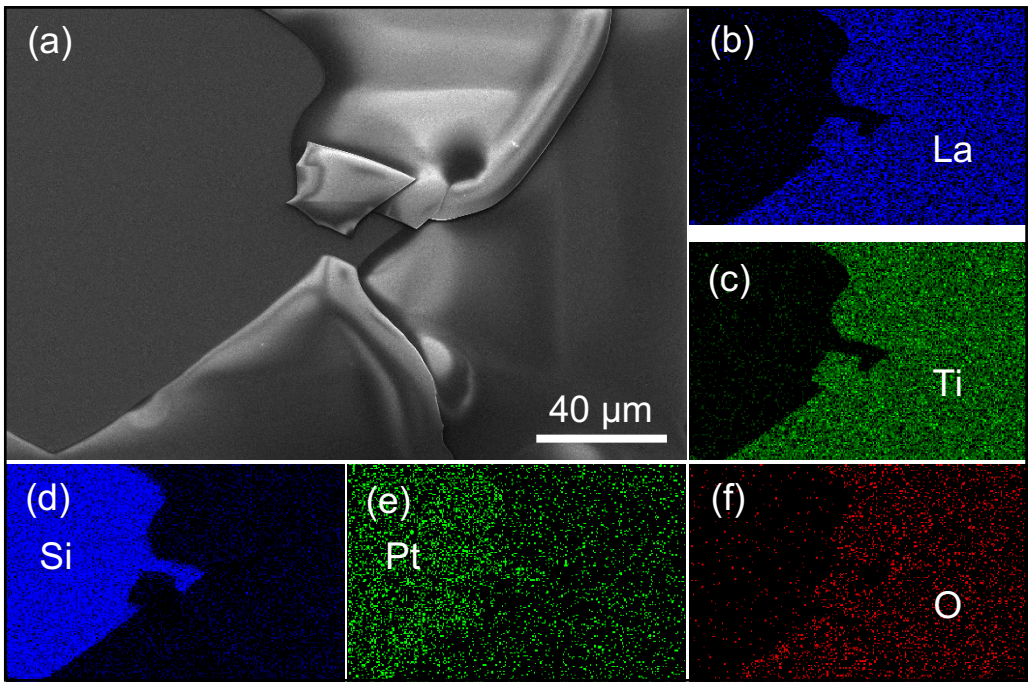

Figure 3.7: An (a) SEM image of LLTO deposited at 15 mTorr. EDS mapping of the region is shown, with signals from (b) La, (c) Ti, (d) Si, (e) Pt, and (f) O. Electron beam voltage was set to 20 keV.

With the morphology issue resolved, EDS spectra were taken from points across the surface of each sample, as shown in Fig. 3.8. There are notable features on the 15 mTorr sample, but the signals gathered throughout the regions were the same regardless of morphology, so only one spectrum is shown. There are clear peaks corresponding to lanthanum, titanium, and oxygen when LLTO is deposited with 15 mTorr and 7.5 mTorr pressure. This indicates that each film contains similar LLTO chemistry. More information can be obtained by taking the lanthanum/titanium ratio of each film. By comparing the film La/Ti ratios to that of the original target material, we can see how the LLTO composition has changed as a result of sputtering and annealing. The film ratios are shown in table 3.2, while the LLTO sputtering target contains a

La/Ti ratio of 0.5. Compared to the sputtering target, both films saw a decreased ratio overall, with there being a clear difference between the film made at 15 mTorr and at 7.5 mTorr. We can determine that changes in deposition pressure influence LLTO film composition.

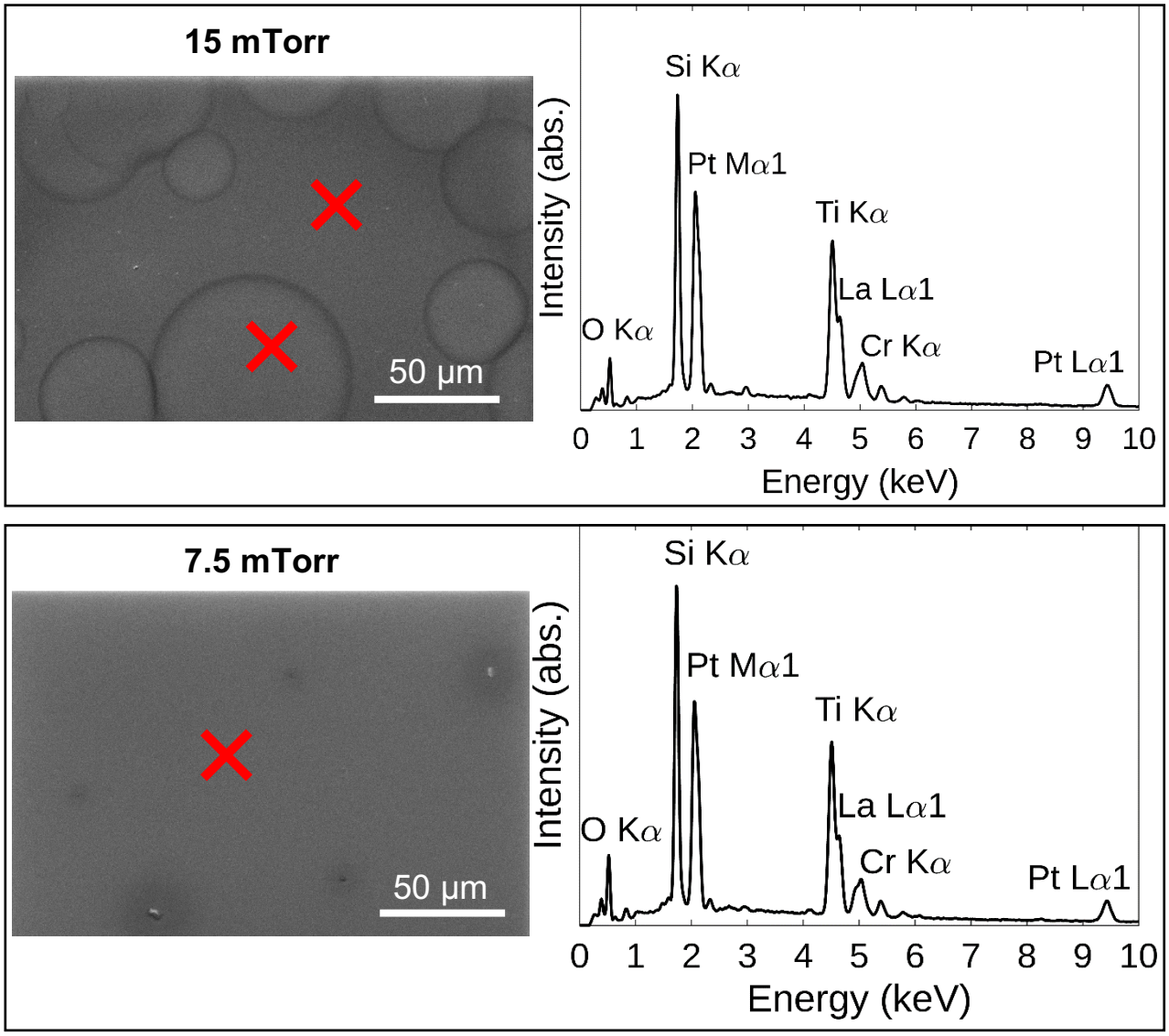

Figure 3.8: Surface SEM images and point EDS spectra of LLTO deposited at (top) 15 mTorr and (bottom) 7.5 mTorr. Electron beam voltage was set to 20 keV.

Table 3.2: La/Ti ratios for LLTO deposited at 15 mTorr and 7.5 mTorr.

Pressure (mTorr)	La/Ti Ratio
15	0.44 ± 0.02
7.5	0.39 ± 0.02

CHAPTER 4. CONCLUSION

Further developments have been made in optimizing the sputter deposition of LiPON and LLTO solid electrolytes. Calibration of LiPON deposition time revealed a linear approximation for the deposition rate, allowing film thickness to be tuned. The electrochemical properties of LiPON are maintained for films of different thickness. Order of magnitude differences between ionic and electronic conductivity values are present even for a 325 nm film, demonstrating the capability of LiPON to improve volumetric energy density in ASSBs. For sputtering LLTO, the decision to use the $Li_{0.68}La_{0.49}TiO_3$ target was made considering the effect of lithium amount on bulk ionic conductivity. Effects of sputtering power and pressure on the LLTO deposition rate were tracked, with sputtering power holding a much greater influence on deposition rate. With CTE mismatch between the Si substrate and LLTO film, annealing had led to delamination, but this issue was resolved by growing thinner films. LLTO films were grown at different pressures, and EDS analysis unveiled a difference in La/Ti ratio. This indicates that changing the deposition pressure can change LLTO film composition. Overall, the special consideration of deposition parameters is essential for fabricating thin film SSEs with favorable morphology and strong electrochemical properties.

APPENDIX

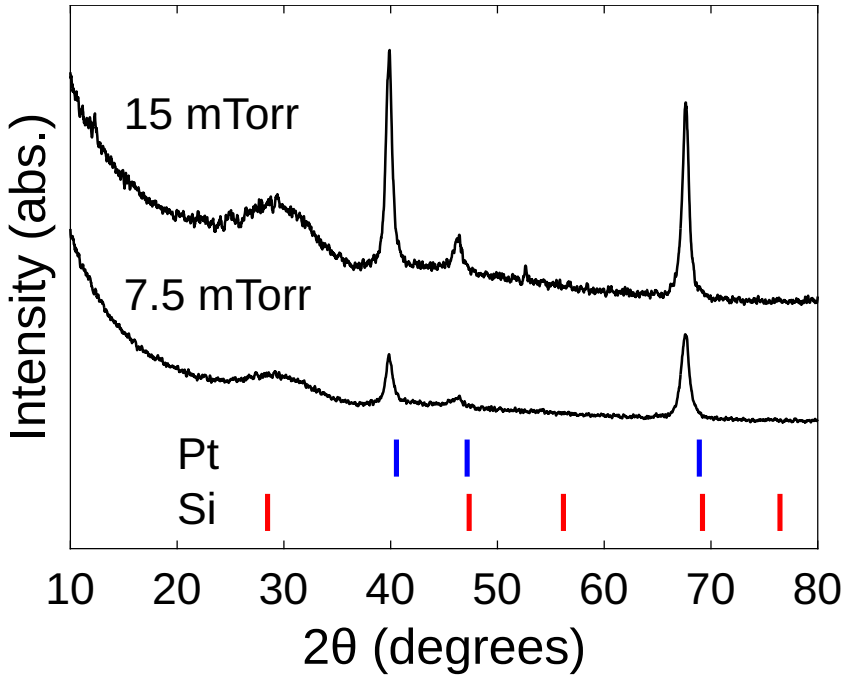

Figure A.1. XRD data of LLTO films deposited at 15 mTorr and 7.5 mTorr. The sharp peaks are attributed to the substrate material, meaning each film displays amorphous structure.

REFERENCES

1. Moitzheim, S., Put, B., & Vereecken, P. M. (2019). Advances in 3D thin-film Li-ion batteries. *Advanced Materials Interfaces*, *6*(15), 1900805.

2. Xia, Q., Zan, F., Zhang, Q., Liu, W., Li, Q., He, Y., Hua, J., Liu, J., Xu, J., Wang, J., Wu, C., & Xia, H. (2023). All-Solid-State Thin Film Lithium/Lithium-Ion Microbatteries for Powering the Internet of Things. *Advanced Materials*, *35*(2), 2200538.

3. Cheng, D., Wynn, T. A., Wang, X., Wang, S., Zhang, M., Shimizu, R., Bai, S., Nguyen, H., Fang, C., Kim, M., Li, W., Lu, B., Kim, S. J., & Meng, Y. S. (2020). Unveiling the stable nature of the solid electrolyte interphase between lithium metal and LiPON via cryogenic electron microscopy. *Joule*, *4*(11), 2484-2500.

4. Su, Y., Falgenhauer, J., Polity, A., Leichtweiß, T., Kronenberger, A., Obel, J., Zhou, S., Schlettwein, D., Janek, J., & Meyer, B. K. (2015). LiPON thin films with high nitrogen content for application in lithium batteries and electrochromic devices prepared by RF magnetron sputtering. *Solid State Ionics*, *282*, 63-69.

5. Wang, H., Wang, J., Shi, Q., Su, Y., Tang, P., Huang, S., Lin, S., & Dai, M. (2023). Influence of LiPON thickness on the electro-optical performance of inorganic all-solid-state electrochromic devices. *Solar Energy Materials and Solar Cells*, *251*, 112140.

6. Lee, J. Z., Wang, Z., Xin, H. L., Wynn, T. A., & Meng, Y. S. (2016). Amorphous lithium lanthanum titanate for solid-state microbatteries. *Journal of the Electrochemical Society*, *164*(1), A6268.

7. Song, S. P., Yang, C., Jiang, C. Z., Wu, Y. M., Guo, R., Sun, H., Yang, J. L., & Zhang, X. K. (2022). Increasing ionic conductivity in Li0. 33La0. 56TiO3 thin-films via optimization of processing atmosphere and temperature. *Rare Metals*, *41*(1), 179-188.

8. Xiong, Y., Tao, H., Zhao, J., Cheng, H., & Zhao, X. (2011). Effects of annealing temperature on structure and opt-electric properties of ion-conducting LLTO thin films prepared by RF magnetron sputtering. *Journal of Alloys and Compounds*, 509(5), 1910-1914.

9. Song, S., Peng, X., Huang, K., Zhang, H., Wu, F., Xiang, Y., & Zhang, X. (2020). Improved cycling stability of LiCoO2 at 4.5 V via surface modification of cathode plates with conductive LLTO.

10. Chen, R., Liang, W., Zhang, H., Wu, F., & Li, L. (2012). Preparation and performance of novel LLTO thin film electrolytes for thin film lithium batteries. *Chinese Science Bulletin*, 57, 4199-4204.

11. Blackman, J. A., & Wilding, A. (1991). Scaling theory of island growth in thin films. *Europhysics Letters*, *16*(1), 115.

12. Zhou, X., Gao, C., Wang, D., Peng, S., Huang, L., Yang, W., Zhang W. H., & Gao, X. (2022). Revealing the dominant factor of domain boundary resistance on bulk conductivity in lanthanum lithium titanates. *Journal of Energy Chemistry*, *73*, 354-359.

13. Bertrand, M., Rousselot, S., Aymé-Perrot, D., & Dollé, M. (2021). Compatibility assessment of solid ceramic electrolytes and active materials based on thermal dilatation for the development of solid-state batteries. *Materials Advances*, 2(9), 2989-2999.

14. Schoedel, R., & Boensch, G. (2001). Precise interferometric measurements at single-crystal silicon yielding thermal expansion coefficients from 12 deg to 28 degC and compressibility. *In Recent Developments in Traceable Dimensional Measurements* (Vol. 4401, pp. 54-62). SPIE.

15. Kuscer, D., Bantan, I., Hrovat, M., & Malič, B. (2017). The microstructure, coefficient of thermal expansion and flexural strength of cordierite ceramics prepared from alumina with different particle sizes. *Journal of the European Ceramic Society*, 37(2), 739-746.